ACS APPLIED MATERIALS & INTERFACES

Surfaces, Interfaces, and Applications

Design of 3D Porous Structure with Residual Carbon for High-Performance Ni-Rich Cathode Materials

Hang Dong, Guobiao Liu, Shaomin Li, Sixu Deng, Yanhua Cui, Heng Liu, Hao Liu, and Xueliang Sun

ACS Appl. Mater. Interfaces, **Just Accepted Manuscript** • DOI: 10.1021/acsami.8b17800 • Publication Date (Web): 03 Dec 2018

Design of 3D Porous Structure with Residual Carbon for High-Performance Ni-Rich Cathode Materials

Hang Dong [1, 2], Guobiao Liu[3]*, Shaomin Li [1], Sixu Deng[4], Yanhua Cui[5], Heng Liu[2], Hao Liu [1, *], Xueliang Sun[4]

[1]Chengdu Green Energy and Green Manufacturing Technology R&D Center, Chengdu Development Center of Science and Technology, China Academy of Engineering Physics, Chengdu, 610200, China

[2]College of Materials Science and Engineering, Sichuan University, Chengdu 610064, China

[3]Department of Materials Science, Sichuan Engineering Technical College, Deyang 618000, China

[4]Department of Mechanical and Materials Engineering, University of Western Ontario, London, Ontario N6A 5B9, Canada

[5]Institute of Electronic Engineering, China Academy of Engineering Physics, Mianyang 621000, PR China

*Corresponding author: Guobiao Liu E-mail address: guobiaoliu@sina.com

ORCID：0000-0002-8223-3128

Hao Liu E-mail address: mliuhao@gmail.com

ORCID：0000-0002-6284-4183

Keyword: Lithium-ion battery, Ni-rich cathode material, $LiNi_{0.8}Co_{0.1}Mn_{0.1}O_2$, sol-gel, 3D-porous morphology, residual carbon.

Abstract

Recently, $LiNi_{0.8}Co_{0.1}Mn_{0.1}O_2$ has drawn much attention due to its high energy density. Here 3D-porous $LiNi_{0.8}Co_{0.1}Mn_{0.1}O_2$ and one with residual carbon have been synthesized using a resorcinol-formaldehyde assisted sol-gel approach. SEM images

verify that the synthesized $LiNi_{0.8}Co_{0.1}Mn_{0.1}O_2$ possesses a 3D-porous morphology. XPS analysis and TEM-mapping images indicate the existence of residual carbon in the secondary particle of 3D-porous $LiNi_{0.8}Co_{0.1}Mn_{0.1}O_2$. Furthermore, 3D-porous $LiNi_{0.8}Co_{0.1}Mn_{0.1}O_2$ with residual carbon exhibits outstanding electrochemical properties. At a current density of 1900 mA g^{-1}, the 3D-porous $LiNi_{0.8}Co_{0.1}Mn_{0.1}O_2$ with residual carbon can still deliver a reversible capacity of 113 mAh g^{-1}. Moreover, after 150 cycles at 0.2 C, the capacity retention of 3D-porous $LiNi_{0.8}Co_{0.1}Mn_{0.1}O_2$ with residual carbon reaches to 95%. The excellent electrochemical properties can be ascribed to the unique 3D-porous morphology and residual carbon in the secondary particle.

1. Introduction

Over the past decade, Ni-rich layered oxides ($LiNi_{1-x-y}Co_xTM_yO_2$, TM = Mn or Al), as one of the most successful cathode materials for lithium ion batteries (LIBs), has drew much attention owing to the advantages of high practical specific energy (excess 720 Wh kg^{-1} originated from the high practical reversible capacity of ~200 mAh g^{-1} and high discharge voltage of 3.7 V), cheapness and low toxicity[1-4]. To date, Ni-rich layered oxides have been successfully used as cathode materials for power LIBs with excellent electrochemical properties[5-6]. However, as cathode materials for power LIBs, Ni-rich layered oxides are expected to deliver more excellent electrochemical properties[7-10].

A large amount of work has been done to further enhance electrochemical property of Ni-rich layered oxides. So far, morphology controlling, surface

modification and a combination of morphology controlling and surface modification are proved to be useful strategies[11-14]. For example, Ni-rich layered oxides with nano-sized primary particles usually demonstrate improved rate capability because the nano-sized primary particles are beneficial to Li^+ insertion/deinsertion by shortening Li^+ diffusion pathways[15]. Ni-rich layered oxides with surface coating generally display enhanced cyclic performance since the surface coating is helpful to the formation of stable solid electrolyte interface (SEI) film[16]. Nano-sized Ni-rich layered oxides with surface coating showed improved rate capability and cyclic performance due to the combination of shortening Li^+ diffusion pathways and forming stable SEI film[17].

Besides modifying surface and decreasing the primary particle size, constructing 3D-porous structure is another effective strategy to enhance the electrochemical properties. The mechanism can be described as follows. Firstly, the 3D-porous structure is helpful to electrolyte penetration into the core of secondary particle, which provides more points for Li^+ to diffuse into electrolyte[18]. This contributes to the improvement of rate capability. Secondly, the volume expansion of the primary particles during cycling is confirmed to be a source of poor cycling stability. The porosities of in the secondary particle with 3D-porous structure can serve as a buffer space, which contributes to the enhancement of cyclic performance. Owing to above-mentioned advantage of 3D-porous structure, many works are focused on preparing cathode materials with 3D-porous structure[19-22]. Bruce et al synthesized $Li[Li_{0.2}Ni_{0.2}Mn_{0.6}]O_2$ with porous morphology using sol-gel method. The prepared

material demonstrates an excellent cyclic performance[23]. Up to now, to our knowledge, there is no work about preparing the $LiNi_{0.8}Co_{0.1}Mn_{0.1}O_2$ with 3D-porous structure.

In this work, $LiNi_{0.8}Co_{0.1}Mn_{0.1}O_2$with 3D-porous structure has been prepared by a resorcinol-formaldehyde assisted sol-gel approach. Moreover, by controlling burning condition, 3D-porous $LiNi_{0.8}Co_{0.1}Mn_{0.1}O_2$ with residual carbon has been prepared. The prepared cathode powder with residual carbon demonstrates a highly improved rate capability with 113 mAh g^{-1} at 10 C and enhanced cycling performance with capacity retention of 95% after 150 cycles.

2. Experimental

The target product was fabricated using a resorcinol-formaldehyde assisted sol-gel approach, since resorcinol and formaldehyde has been widely used in the synthesis of porous materials[22]. As shown in Fig. 1, based on the formula of $LiNi_{0.8}Co_{0.1}Mn_{0.1}O_2$, nickel acetate, cobalt acetate, manganese acetate and lithium carbonate (5% excess) were dissolved together. Then resorcinol and formaldehyde were added into solution. As shown in Fig. S1, a polymerization reaction occurred by hydrogen bond and carbonyl. A chelate the ions reaction occurred by hydrogen bond and metal ions. After more than 3 hours of agitation at 60 °C, the mixture became a colloid. After that, the dried colloid was burned at 500 °C for 5 h and 765 °C for 8 h under O_2 at mosphere with a gas-flow of 50 ml/min. As-prepared material was denoted as 3D-LNCM. The 3D-porous $LiNi_{0.8}Co_{0.1}Mn_{0.1}O_2$ with residual carbon was obtained at a burning condition of O_2 atmosphere with a gas-flow of 5 ml/min.

As-prepared material was denoted as 3D-LNCM/C.

The structure was characterized by X-ray diffraction (XRD) testing. The morphology and particle size were observed through scanning electron microscopy (SEM) measurements. The element distribution was observed by conducting energy-dispersive X-ray spectrometer (EDX) tests. The composition was verified by conducting inductively coupled plasma (ICP) measurements. The surface property was characterized by X-ray photoelectron spectroscopy (XPS). High resolution transmission electron microscope (HR-TEM) and its mapping images were gotten to verify the element distribution and specific crystallographic planes. The pore property of samples was characterized by gas sorption analysis and mercury intrusion analysis. The content of carbon element in samples was detected by high frequency infrared carbon sulfur analyzer. The electronic conductivity of samples was measured on 4-point probes resistivity measurement system (Four Probes Tech, RTS-9) using powder pressed into disks.

The electrochemical performance of prepared cathode powder was tested using half cells with a lithium foil as negative electrode. The cell packaging steps are consistent with that in previous literature[13]. The preparation of electrode is as follows. 80 wt% active materials, 10 wt% acetylene black and 10 wt% polyvinylidene fluoride were blended using N-methyl pyrrolidone as a solvent. Then the mixture was coated on an aluminum foil. The electrode sheet was dried at a vacuum drying oven for 12 h. Then the electrode sheet was cut into small disks with about 2 cm^2. The active material loading mass is limited around 6.0 mg cm^{-2}. The charge-discharge tests were

operated on cell test instruments (LAND CT-2001A). The voltage ranges from 2.8 to 4.3 V. And the temperature is about 25 °C. The impedance tests of cells were carried out on the Parstat 4000 electrochemical workstation. The frequencies ranges from 100 kHz to 0.01Hz and the fluctuation voltage is 5 mV.

3. Results and discussion

Fig. 2a-d displays the SEM images of 3D-LNCM and 3D-LNCM/C at different magnifications. As shown in Fig. 2a and b, 3D-LNCM/C prepared by the resorcinol-formaldehyde assisted sol-gel method demonstrates a desirable 3D porous morphology. Many pores with diameter of 1.0−3.0 μm can be observed in the secondary particle and the size of the secondary particles ranges from 3−30 μm. As shown in Fig. 2c and d, 3D-LNCM possesses similar hierarchical morphology. The SEM images of spherical $LiNi_{0.8}Co_{0.1}Mn_{0.1}O_2$ (denoted as S-LNCM) prepared by conventional co-precipitation method following the calcination in atmosphere of flowing oxygen are also provided and shown in Fig. S2a and b. An obvious spherical morphology is observed. The size of the secondary particles ranges from 8 to 15 μm. In contrast to many pores in the secondary particles of 3D-LNCM and 3D-LNCM/C, there are no obvious pores in the secondary particles of S-LNCM. As reported in previous literatures[24-26], the gaps and voids in Ni-rich cathode can promote electrolyte infiltration, which is benefit for Li^+ transport and electronic delivery. Therefore, the gaps and voids in Ni-rich cathode can improve the rate performance of Ni-rich layered cathode materials. Besides, the gaps and voids between the primary particles can alleviate the structure stress which was accompanied by cycle processes. Hence,

3D-LNCM and 3D-LNCM/C, which possess rich pore structure, have more excellent electrochemical property comparing to spherical cathode powder.

Fig. 2e shows the XRD patterns of 3D-LNCM and 3D-LNCM/C. The main peaks can be indexed as hexagonal $LiNiO_2$ structure with $R\bar{3}m$ space group which is similar to reported results in previous literatures[27]. In addition, both XRD patterns show clear splitting (006)/(012) and (108)/(110) peaks, suggesting a good crystallinity of layered structure in these samples[28]. S-LNCM powder also has similar XRD pattern (Fig.S2c). As listed in Table S1, the $I_{(003)}/I_{(104)}$ intensity ratios for S-LNCM, 3D-LNCM and 3D-LNCM/C were 1.656, 1.642, and 1.605, respectively, indicating that all samples have the quite small Li^+/Ni^{2+} disorder. This analysis result of XRD patterns illustrates that the resorcinol-formaldehyde assisted sol-gel approach can be used to synthesis $LiNi_{0.8}Co_{0.1}Mn_{0.1}O_2$ with a good crystallinity.

In order to investigate the effect of different methods on the chemical compositions of as-prepared powders, ICP is used to detect the content of Li, Ni, Co and Mn elements in cathode powders. As listed in Table S2, these samples have similar calculated atomic ratios of Li, Ni, Co and Mn elements. Moreover, EDX-mapping images (Fig. S3) were obtained to verify the dispersal uniformity of Ni, Co and Mn elements in three different samples. Fig. S3 confirms that Ni, Co and Mn elements are distributed homogeneously, which implied that $LiNi_{0.8}Co_{0.1}Mn_{0.1}O_2$ with uniform dispersion of Ni, Co and Mn elements can be prepared by the resorcinol-formaldehyde assisted sol-gel approach.

The surface and pore properties of S-LNCM, 3D-LNCM and 3D-LNCM/C were

characterized by both mercury porosimetry and monosorb surface area analyzer. As shown in Fig. 3a, the pore size distribution curve of 3D-LNCM demonstrates a steep peak at 2 μm. The pore size distribution curve of 3D-LNCM/C is similar to that of 3D porous cathode powder with exception of higher broad peak between 0.1 to 1 μm. This peak is supposed to be related to small pores caused by residual carbon. As shown in Fig. S4a, the pore size distribution curve of S-LNCM only presents a peak at 3 μm which can be ascribed to micro-sized pores caused by the secondary particle clearance. Table S3 shows the specific surface area of three samples measured with mercury intrusion porosimetry. 3D-LNCM/C possesses the biggest specific surface area (2.3138 m^2 g^{-1}) while S-LNCM has the smallest specific surface area (0.3705 m^2 g^{-1}). To achieve detailed pore structure information in sub-micrometer range, the pore size distribution was also tested by monosorb surface area analyzer. As shown in Fig. 3b, the pore size distribution curve of 3D-LNCM/C shows an obvious peak at 9 nm while those of 3D-LNCM and S-LNCM (Fig. S4b) show no clear peak in that range. This peak at 9 nm is related to mesopore on residual carbon. The specific surface area results tested by monosorb surface area analyzer are listed in Table S4. The results show a similar trend as observed from mercury intrusion porosimetry test. Both results show that 3D-LNCM/C has the biggest specific surface area among the three samples. This result should originate from the gap between amorphous residual carbon and electrode material, which can effectively increase the specific surface area. Similar phenomenon has also been observed from carbon-coated $LiFePO_4$ cathode[29].

XPS spectra were obtained to analyze the surface properties of the primary particles of 3D-LNCM and 3D-LNCM/C. Since XPS is a surface sensitive measurement, and the residual carbon might be present in the middle of the secondary particle of 3D-LNCM/C rather than on the surface, all XPS tests were conducted on grinded sample in order to make sure the residual carbon in the secondary particle can be detected. The morphology of the grinded sample is shown in Fig. S5b. The XPS spectra of both samples are demonstrated in Fig. 4 and Fig. S6. The C1s spectrum of 3D-LNCM shows two peaks at 284.3 and 289.2 eV. These two peaks are in accord to those of hydrocarbon contaminations and Li_2CO_3 reported in previous literature[30], indicating no residual carbon exists in 3D-LNCM. However, the C1s spectrum of 3D-LNCM/C can be fitted with four peaks which are located at 284.3, 286.0, 288.0 and 289.2 eV, respectively[31-33]. Besides the peaks assigned to hydrocarbon contaminations and Li_2CO_3 at 284.3 and 289.2 eV, the other two peaks positioned at 286.0 and 288.0 eV can be attributed to C-C and O-C=O (alkyl carbonates) bonds, respectively. It can be assumed that amorphous carbon was left over in the secondary particles of 3D-LNCM/C. The result is also supported by the comparison between Ni $2p_{3/2}$ spectra of the two samples. As depicted in Fig. 4b, the best fit for the Ni $2p_{3/2}$ spectrum give two peaks at 855.0 and 857.0 eV, respectively. As reported in the previous literatures[30, 34-35], the strong peak at 855.0 eV can be explained by the existence of Ni^{2+}. The other one at 857.0 eV can be attributed to Ni^{3+}. Comparing to 3D-LNCM, 3D-LNCM/C possesses a weaker peak at 857.0 eV, which might be related to the reduction of part Ni^{3+} due to decomposition of organics under less

oxygen condition. This speculation is in accord with analyses about the $I_{(003)}/I_{(104)}$ intensity ratios for S-LNCM, 3D-LNCM and 3D-LNCM/C. As listed in Table S1, the intensity ratio of $I_{(003)}/I_{(104)}$ for 3D-LNCM/C is slight lower than that for S-LNCM and 3D-LNCM, indicating a slight increase of cation mixing layer for 3D-LNCM/C. The slight increase of cation mixing layer for 3D-LNCM/C can be ascribed to the reduction of part Ni^{3+} into Ni^{2+}. It is well known that the Ni^{2+} easily causes the cation mixing layer.

To further investigate the structure and surface properties of 3D-LNCM/C, TEM，TEM-EDX mapping and HR-TEM images were used. As shown in TEM image (Fig.5a), some small regions with light color are observed in the middle of big black particle, indicating a porous structure. TEM-EDX mapping of 3D-LNCM/C (Fig.5c-d) shows the existence of C, Ni, Co and Mn elements in 3D-LNCM/C. This result is consistent with the presence of C-C bond observed from XPS analysis. Furthermore, high frequency infrared carbon sulfur analyzer was used to detect the content of carbon element in 3D-LNCM/C material. The content of carbon element is as low as 1.92%. HR-TEM mapping image (Fig. 5b) also demonstrates some amorphous particles near the edge of 3D-LNCM/C. Clear lattice fringes, as shown in Fig.5g, are observed. The distance between two adjacent lattice is 4.7 Å, corresponding to the space of two [003] planes of layered cathode material[36-38]. The TEM and HR-TEM images of other sample are shown in Fig. S7 of the Supporting Information, and the main patterns are similar to 3D-LNCM/C.

The electrochemical behaviors of three samples are shown in Fig. 6. All

electrochemical results were gotten in the voltage range of 2.8-4.3 V at room temperature. Fig. 6a shows the first charge/discharge curves at 0.1C. The behavior of three samples are similar to results of comparable Ni-rich electrodes in others' reports[47,48]. The capacities are lower than theoretical capacity of 280 mAh g^{-1} [34]. The Ni^{2+}/Ni^{4+} and Co^{3+}/Co^{4+} oxidation-reduction reaction peaks are clearly shown in three dQ/dV curves (Fig. S8a, b, and c). Among three samples, 3D-LNCM/C has the largest reversible capacity. Furthermore, 3D-LNCM/C has the best rate capability of 113 mAh g^{-1} at 10 C (a current density of 1900 mA g^{-1}) and cyclic performance of 95% capacity retention after 150 cycles. In addition, 3D-LNCM/C displays the slightest voltage decay (shown in Fig.S9). These outstanding performances can be attributed to the combined action of the hierarchical morphology and residual carbon. The hierarchical 3D morphology has an advantage of giving more points for Li^+ diffusion into electrolyte, and the residual carbon is helpful to improve electron conductivity (shown in Fig. S10). These two properties can improve the rate capability. Meanwhile, the 3D-porous structure can offer large space to fit volume expansion of the primary particles. The residual carbon covering on the surface of primary particle can reduce the side reaction between material and electrolyte, which is helpful to build a stable SEI film. The large space for volume expansion and stable SEI film can enhance cycling stability.

EIS tests were conducted to illustrate the electrochemical impedance by using cells which have been charged and discharged for 5 and 150 cycles. Fig. 7 displays the Nyquist plots and magnified Nyquist plots in high frequency area. The impedance

spectra can be explained using an equivalent electrical circuit shown in Fig. 7f which consists of electrolyte resistance (R_s), resistance of solid electrolyte interface film (R_{SEI}), electron transfer impedance (R_e), charge-transfer resistance (R_{ct}), and Warburg impedance (Z_w)[39]. TableS5 shows the specific data of each resistance. As demonstrated in previous literature[40], the R_{SEI} and R_{ct} values increase during subsequent cycles. Compared to S-LNCM and 3D-LNCM, 3D-LNCM/C demonstrates the lowest R_{SEI} and R_{ct} values after 5 and 150 cycles. Furthermore, after 150 cycles, the increase of R_{SEI} and R_{ct} values of 3D-LNCM/C is small, indicating a stable SEI film for 3D-LNCM/C.

Based on Warburg impedance in the low frequency region and following equation, the Li^+ diffusion coefficient of electrode has been calculated [41-43]:

$$D = 0.5R^2T^2A^{-2}n^{-4}F^{-4}C^{-2}B^{-2}$$

The equation parameters include the gas constant (R), the absolute temperature (T), the surface area of the cathode (A), the number of electrons permolecule during oxidization (n), the Faraday constant (F), the concentration of lithium ion (C) and the Warburg factor (B), which can be calculated by following equation:

$$Re(Z_\omega) = B\omega^{-1/2}$$

As shown in Fig. 7c, in the low frequency region, squarer root of frequency ($\omega^{-1/2}$) and Z_{re} are in a linear relationship. The lithium ion diffusion coefficients are listed in Table S5. The lithium ion diffusion coefficient of 3D-LNCM/C is much higher than those of the other two samples, which is in accordance with the good rate capability of 3D-LNCM/C.

4. Conclusion

In conclusion, 3D-porous $LiNi_{0.8}Co_{0.1}Mn_{0.1}O_2$ with residual carbon can be synthesized by sol-gel approach using resorcinol-formaldehyde as chelating agent. The unique 3D-porous structure can effectively relieve volume expansion and promote electrolyte infiltration, which is benefit to the improvement of rate capability and cyclic performance. The residual carbon on 3D-porous $LiNi_{0.8}Co_{0.1}Mn_{0.1}O_2$ is helpful to improve electron conductivity and build a stable SEI film, which has positive effects on electrochemical performance improvement. The reversible capacity of 3D-LCNM/C can reach as high as 113 mAh g^{-1} at 10 C and the capacity retention is 95% after 150 cycles at 0.2 C. These findings confirm the possibility of forming some residual carbon in the secondary particle by controlling the burning condition in the process of preparing 3D-porous$LiNi_{0.8}Co_{0.1}Mn_{0.1}O_2$ through resorcinol-formaldehyde assisted sol-gel approach. These results also reveal the importance of residual carbon on electrochemical properties of Ni-rich layered oxides.

Acknowledgement

The research was financially supported by the Funding of LPMT (Laboratory of Precision Manufacturing), CAEP (ZD17006), the Sichuan Provincial Key Technology R&D Program (2016GZ0299).

Associated Content

The Supporting Information is available free of charge on the ACS Publications website. 1. Images, schematic diagram about the function of resorcinol and formaldehyde; additional SEM, EDX-mapping and HR-TEM images; additional XRD patterns, pore size distribution curves and XPS spectra of samples; additional

electrochemical properties. 2. Tables, XRD parameters and element molar ratios of samples; specific surface area data; values of diffusion coefficient and resistance; comparison of electrochemical performances of Ni-rich cathode materials.

References

(1) Liu, W.; Oh, P.; Liu, X.; Lee, M. J.; Cho, W.; Chae, S.; Kim, Y.; Cho, J. Nickel-Rich Layered Lithium Transition-Metal Oxide for High-Energy Lithium-Ion Batteries. Angew. Chem. Int. Ed. Engl. **2015**, 54, 4440-4457.

(2) Hou, P.; Yin, J.; Ding, M.; Huang, J.; Xu, X. Surface/Interfacial Structure and Chemistry of High-Energy Nickel-Rich Layered Oxide Cathodes: Advances and Perspectives. Small **2017**, 13, 1701802.

(3) Manthiram, A.; Song, B.; Li, W. A Perspective on Nickel-Rich Layered Oxide Cathodes for Lithium-Ion Batteries. Energy Storage Mater. **2017**, 6, 125-139.

(4) Kim, T.-H.; Park, J.-S.; Chang, S. K.; Choi, S.; Ryu, J. H.; Song, H.-K. The Current Move of Lithium Ion Batteries Towards the Next Phase. Adv. Energy Mater. **2012**, 2, 860-872.

(5) Myung, S.-T.; Maglia, F.; Park, K.-J.; Yoon, C. S.; Lamp, P.; Kim, S.-J.; Sun, Y.-K. Nickel-Rich Layered Cathode Materials for Automotive Lithium-Ion Batteries: Achievements and Perspectives. ACS Energy Lett. **2016**, 2, 196-223.

(6) Ding, Y.; Mu, D.; Wu, B.; Wang, R.; Zhao, Z.; Wu, F. Recent Progresses on Nickel-Rich Layered Oxide Positive Electrode Materials Used in Lithium-Ion Batteries for Electric Vehicles. Appl. Energy **2017**, 195, 586-599.

(7) Liao, J. Y.; Oh, S. M.; Manthiram, A. Core/Double-Shell Type Gradient Ni-Rich

$LiNi_{0.76}Co_{0.10}Mn_{0.14}O_2$ with High Capacity and Long Cycle Life for Lithium-Ion Batteries. ACS Appl. Mater. Inter. **2016**, 8, 24543-24549.

(8) Zhang, Y.; Shi, H.; Song, D.; Zhang, H.; Shi, X.; Zhang, L. Facile Synthesis of a Novel Structured $Li[Ni_{0.66}Co_{0.1}Mn_{0.24}]O_2$ Cathode Material with Improved Cycle Life and Thermal Stability via Ion Diffusion. J. Power Sources **2016**, 327, 38-43.

(9) Bak, S. M.; Hu, E.; Zhou, Y.; Yu, X.; Senanayake, S. D.; Cho, S. J.; Kim, K. B.; Chung, K. Y.; Yang, X. Q.; Nam, K. W. Structural Changes and Thermal Stability of Charged $LiNi_xMn_yCo_zO_2$ Cathode Materials Studied by Combined in Situ Time-Resolved XRD and Mass Spectroscopy. ACS Appl. Mater. Inter. **2014**, 6, 22594-22601.

(10) Hwang, S.; Kim, S. M.; Bak, S.-M.; Chung, K. Y.; Chang, W. Investigating the Reversibility of Structural Modifications of $Li_xNi_yMn_zCo_{1-y-z}O_2$ Cathode Materials during Initial Charge/Discharge, at Multiple Length Scales. Chem. Mater. **2015**, 27, 6044-6052.

(11) Du, K.; Xie, H.; Hu, G.; Peng, Z.; Cao, Y.; Yu, F. Enhancing the Thermal and Upper Voltage Performance of Ni-Rich Cathode Material by a Homogeneous and Facile Coating Method: Spray-Drying Coating with Nano-Al_2O_3. ACS Appl. Mater. Inter. **2016**, 8, 17713-17720.

(12) Hua, W.; Wu, Z.; Chen, M.; Knapp, M.; Guo, X.; Indris, S.; Binder, J. R.; Bramnik, Natalia N.; Zhong, B.; Guo, H.; Chou, S.; Kang, Y.-M.; Ehrenberg, H. Shape-Controlled Synthesis of Hierarchically Layered Lithium Transition-Metal Oxide Cathode Materials by Shear Exfoliation in Continuous Stirred-Tank Reactors.

J. Mater. Chem. A **2017**, 5, 25391-25400.

(13) Wang, Z.; Liu, H.; Wu, J.; Lau, W.-M.; Mei, J.; Liu, H.; Liu, G. Hierarchical $LiNi_{0.8}Co_{0.15}Al_{0.05}O_2$ Plates with Exposed {010} Active Planes as a High Performance Cathode Material for Li-Ion Batteries. RSC Adv. **2016**, 6, 32365-32369.

(14) Xiao, B.; Sun, X. Surface and Subsurface Reactions of Lithium Transition Metal Oxide Cathode Materials: An Overview of the Fundamental Origins and Remedying Approaches. Adv. Energy Mater. **2018**, 1802057.

(15) Tian, J.; Su, Y.; Wu, F.; Xu, S.; Chen, F.; Chen, R.; Li, Q.; Li, J.; Sun, F.; Chen, S. High-Rate and Cycling-Stable Nickel-Rich Cathode Materials with Enhanced Li^+ Diffusion Pathway. ACS Appl. Mater. Inter. **2016**, 8, 582-587.

(16) Chen, S.; He, T.; Su, Y.; Lu, Y.; Bao, L.; Chen, L.; Zhang, Q.; Wang, J.; Chen, R.; Wu, F. Ni-Rich $LiNi_{0.8}Co_{0.1}Mn_{0.1}O_2$ Oxide Coated by Dual-Conductive Layers as High Performance Cathode Material for Lithium-Ion Batteries. ACS Appl. Mater. Inter. **2017**, 9, 29732-29743.

(17) Kim, J.; Lee, J.; Ma, H.; Jeong, H. Y.; Cha, H.; Lee, H.; Yoo, Y.; Park, M.; Cho, J. Controllable Solid Electrolyte Interphase in Nickel-Rich Cathodes by an Electrochemical Rearrangement for Stable Lithium-Ion Batteries. Adv. Mater. **2017**, 30, 1704309.

(18) He, X.; Wang,J.; Wang,R.; Qiu,B.; Frielinghaus,H.; Niehoff,P.; Liu,H.; Stan,M. C.; Paillard,E.; Winter,M.; Li,J. A 3D Porous Li-Rich Cathode Material with an In Situ Modified Surface for High Performance Lithium Ion Batterieswith Reduced Voltage Decay. J. Mater. Chem. A **2016**, 4, 7230–7237.

(19) Li, J.; Wang, X.; Zhao, J.; Chen, J.; Jia, T.; Cao, C. Porous Lithium Nickel Cobalt Manganese Oxide Hierarchical Nanosheets as High Rate Capability Cathodes for Lithium Ion Batteries. J. Power Sources **2016**, 307, 731-737.

(20) Li, L.; Wang, L.; Zhang, X.; Xue, Q.; Wei, L.; Wu, F.; Chen, R. 3D Reticular $Li_{1.2}Ni_{0.2}Mn_{0.6}O_2$ Cathode Material for Lithium-Ion Batteries. ACS Appl. Mater. Inter. **2017**, 9, 1516-1523.

(21) Xiang, M.; Wu, H.; Liu, H.; Huang, J.; Zheng, Y.; Yang, L.; Jing, P.; Zhang, Y.; Dou, S.; Liu, H. A Flexible 3D Multifunctional MgO-Decorated Carbon Foam@CNTs Hybrid as Self-Supported Cathode for High-Performance Lithium-Sulfur Batteries. Adv. Funct. Mater. **2017**, 1702573.

(22) Liu, X.; Li, S.; Mei, J.; Lau, W.-M.; Mi, R.; Li, Y.; Liu, H.; Liu, L. From Melamine–Resorcinol–Formaldehyde to Nitrogen-Doped Carbon Xerogels with Micro- and Meso-pores for Lithium Batteries. J. Mater. Chem. A **2014**, 2, 14429-14438.

(23) Luo, K.; Roberts, M. R.; Hao, R.; Guerrini, N.; Liberti, E.; Allen, C. S.; Kirkland, A. I.; Bruce, P. G. One-Pot Synthesis of Lithium-Rich Cathode Material with Hierarchical Morphology. Nano Lett. **2016**, 16, 7503-7508.

(24) Kim, J.; Cho, H.; Jeong, H. Y.; Ma, H.; Lee, J.; Hwang, J.; Park, M.; Cho, J. Self-Induced Concentration Gradient in Nickel-Rich Cathodes by Sacrificial Polymeric Bead Clusters for High-Energy Lithium-Ion Batteries. Adv. Energy Mater. **2017**, 7, 1602559.

(25) Zhou, L.; Zhao, D.; Lou, X. $LiNi_{0.5}Mn_{1.5}O_4$Hollow Structures as

High-Performance Cathodes for Lithium-Ion Batteries. Angew. Chem. Int. Ed. Engl. **2012**, 51, 239-241.

(26) Zhang, F.; Liu, T.; Li, M.; Yu, M.; Luo, Y.; Tong, Y.; Li, Y. Multiscale Pore Network Boosts Capacitance of Carbon Electrodes for Ultrafast Charging. Nano Lett. **2017**, 17, 3097-3104.

(27) Yuan, J.; Wen, J.; Zhang, J.; Chen, D.; Zhang, D. Influence of Calcination Atmosphere on Structure and Electrochemical Behavior of $LiNi_{0.6}Co_{0.2}Mn_{0.2}O_2$ Cathode Material for Lithium-Ion Batteries. Electrochim. Acta **2017**, 230, 116-122.

(28) Zhao, J.; Zhang, W.; Huq, A.; Misture, S. T.; Zhang, B.; Guo, S.; Wu, L.; Zhu, Y.; Chen, Z.; Amine, K.; Pan, F.; Bai, J.; Wang, F. In Situ Probing and Synthetic Control of Cationic Ordering in Ni-Rich Layered Oxide Cathodes. Adv. Energy Mater. **2017**, 7, 1601266.

(29) Cheng, F.; Wang, S.; Wang, C.-Y.; Li, W.-C. Interconnected Porous Carbon with Tunable Pore Size as a Model Substrate to Confine $LiFePO_4$ Cathode Material for Energy Storage. Microporous Mesoporous Mater. **2015**, 204, 190-196.

(30) Shaju,K.M.; Subba Rao,G.V.; Chowdari,B.V.R.Performance of Layered $Li(Ni_{1/3}Co_{1/3}Mn_{1/3})O_2$ as Cathode for Li-Ion Batteries. Electrochim. Acta **2002**, 48, 145-151.

(31) Merel,P.; Tabbal,M.; Chaker,M.; Moisa,S.; Margot,J. Direct Evaluation of the sp^3 Content in Diamond-Like-Carbon Films by XPS. Appl. Surface Sci. **1998**, 136, 105-110.

(32) Patsalas,P.; Handrea,M.; Logothetidis,S.; Gioti,M.; Kennou,S.; Kautek,W. A

Complementary Study of Bonding and Electronic Structureof Amorphous Carbon Films by Electron Spectroscopy and Optical Techniques. Diamond Relat. Mater. **2001**, 10, 960-964.

(33) Guo, R.; Shi, P.; Cheng, X.; Du, C. Synthesis and Characterization of Carbon-Coated $LiNi_{1/3}Co_{1/3}Mn_{1/3}O_2$ Cathode Material Prepared by Polyvinyl Alcohol Pyrolysis Route. J. Alloys Compd. **2009**, 473, 53-59.

(34) Wu, F.; Tian, J.; Su, Y.; Wang, J.; Zhang, C.; Bao, L.; He, T.; Li, J.; Chen, S. Effect of Ni^{2+}Content on Lithium/Nickel Disorder for Ni-rich Cathode Materials. ACS Appl. Mater. Inter. **2015**, 7, 7702-7708.

(35) Huang, B.; Li, X.; Wang, Z.; Guo, H.; Shen, L.; Wang, J. A Comprehensive Study on Electrochemical Performance of Mn-Surface-Modified $LiNi_{0.8}Co_{0.15}Al_{0.05}O_2$ Synthesized by an In Situ Oxidizing-Coating Method. J. Power Sources **2014**, 252, 200-207.

(36) Wu, N.; Zhang, Y.; Wei, Y.; Liu, H.; Wu, H. Template-Engaged Synthesis of 1D Hierarchical Chainlike $LiCoO_2$ Cathode Materials with Enhanced High-Voltage Lithium Storage Capabilities. ACS Appl. Mater. Inter. **2016**, 8, 25361-25368.

(37) Zeng, J.; Cui, Y.; Qu, D.; Zhang, Q.; Wu, J.; Zhu, X.; Li, Z.; Zhang, X. Facile Synthesis of Platelike Hierarchical $Li_{1.2}Mn_{0.54}Ni_{0.13}Co_{0.13}O_2$ with Exposed {010} Planes for High-Rate and Long Cycling-Stable Lithium Ion Batteries. ACS Appl. Mater. Inter. **2016**, 8, 26082-26090.

(38) Li, J.; Yao, R.; Cao, C. $LiNi_{1/3}Co_{1/3}Mn_{1/3}O_2$Nanoplates with {010} Active Planes Exposing Prepared in Polyol Medium as a High-Performance Cathode for Li-Ion

Battery. ACS Appl. Mater. Inter. **2014**, 6, 5075-5082.

(39) Shin, H.-S.; Shin, D.; Sun, Y.-K. Improvement of Electrochemical Properties of $Li[Ni_{0.4}Co_{0.2}Mn_{0.4-x}Mg_x]O_{2-y}F_y$ Cathode Materials at High Voltage Region. Electrochim. Acta **2006**, 52, 1477-1482.

(40) Liu, G.; Li, S.; Mei, J.; Liu, L.-M.; Cui, Y.; Liu, H. New insights into low temperature properties of Li-rich layered cathode materials. J. Power Sources **2017**, 353, 51-57.

(41) Liu, H.; Li, C.; Zhang, H. P.; Fu, L. J.; Wu, Y. P.; Wu, H. Q. Kinetic Study on $LiFePO_4$/C Nanocomposites Synthesized by Solid State Technique. J. Power Sources **2006**, 159, 717-720.

(42) Xia, Y.; Zhang, W.; Huang, H.; Gan, Y.; Li, C.; Tao, X. Synthesis and Electrochemical Properties of Nb-Doped $Li_3V_2(PO_4)_3$/C Cathode Materials for Lithium-Ion Batteries. Mater. Sci. Eng. B **2011**, 176, 633-639.

(43) Gao, C.; Liu, H.; Liu, G.; Zhang, J.; Wang, W. High-Rate Performance of $xLiFePO_4 \cdot yLi_3V_2(PO_4)_3$/C Composite Cathode Materials Synthesized via Polyol Process. Mater. Sci. Eng. B **2013**, 178, 272-276.

List of figure captions

Fig. 1. A schematic diagram of preparing 3D porous $LiNi_{0.8}Co_{0.1}Mn_{0.1}O_2$ with residual carbon.

Fig. 2. SEM images (a-d) and XRD patterns (e) of 3D-LNCM/C (a, b) and 3D-LNCM (c, d).

Fig. 3. Pore size distribution curves obtained by (a) mercury intrusion method and (b) nitrogen absorption method for 3D-LNCM and 3D-LNCM/C.

Fig. 4. XPS spectra for C (a), Ni (b) of 3D-LNCM (bottom) and 3D-LNCM/C (upper).

Fig. 5. TEM (a, b), TEM-EDX (c,d) mapping and HR-TEM (e-g) images of 3D-LNCM/C.

Fig. 6. Electrochemical properties of 3D-LNCM/C, 3D-LNCM and S-LNCM: (a)

initial charge-discharge curves at 0.1 C, (b) rate capability, (c) cyclic performanceat 0.2C and (d, e,f) charge-discharge curves at 0.2 C at 1st, 50th, 100th and 150 th cycles.

Fig. 7. (a) Nyquist plots of S-LNCM, 3D-LNCM and 3D-LNCM/C after 5 cycles, (b) The relationship between Zre and $\omega^{-1/2}$ at low frequencies after 5 cycles, (c) Nyquist plots after 150 cycles, (d) The relationship between Zre and $\omega^{-1/2}$ at low frequencies after 150 cycles, (e) Nyquist plots at high frequency region after 150 cycles, (f) a corresponding equivalent circuit.

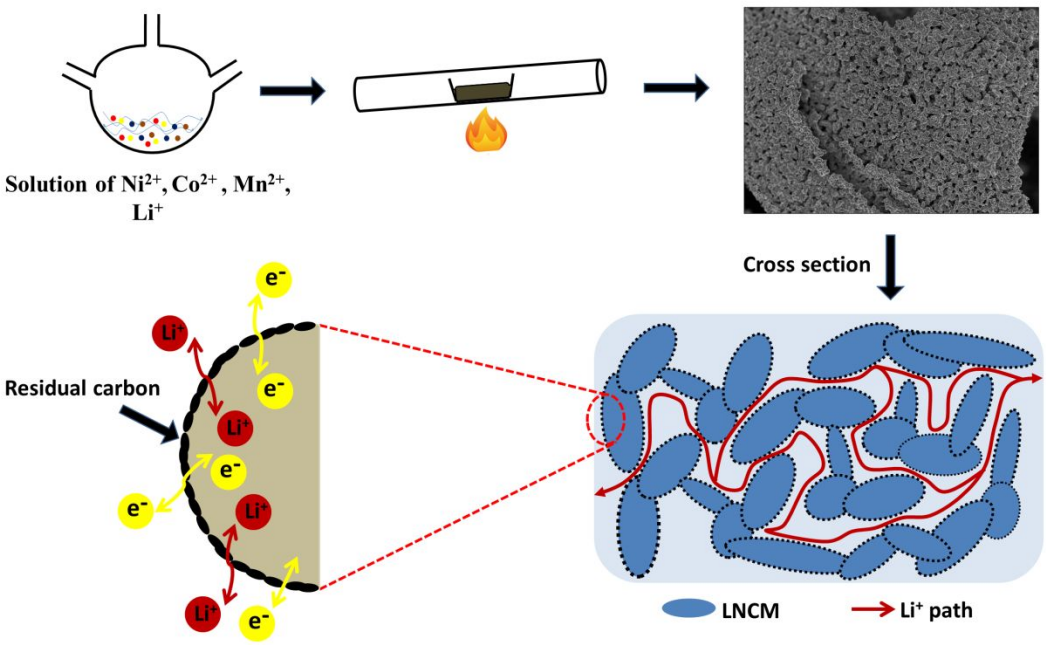

Fig. 1. A schematic diagram of preparing 3D porous $LiNi_{0.8}Co_{0.1}Mn_{0.1}O_2$ with residual carbon.

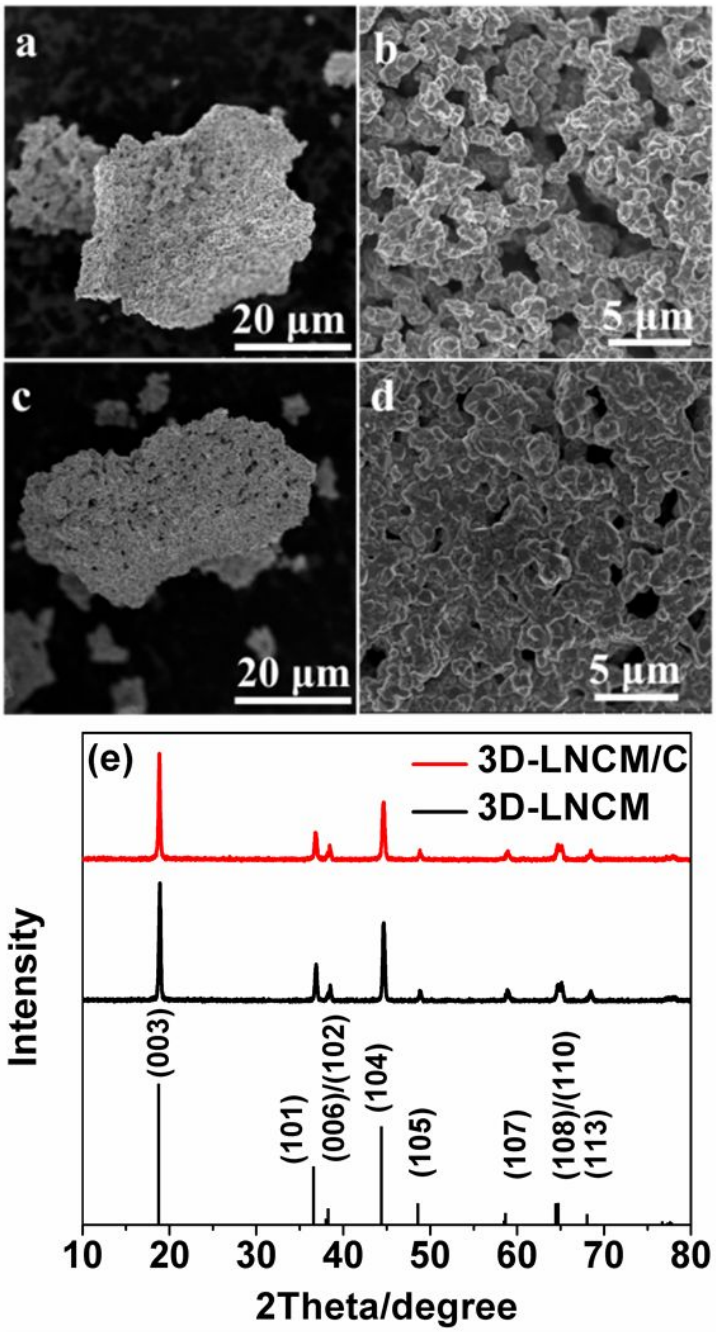

Fig. 2. SEM images (a-d) and XRD patterns (e) of 3D-LNCM/C (a, b) and 3D-LNCM (c, d).

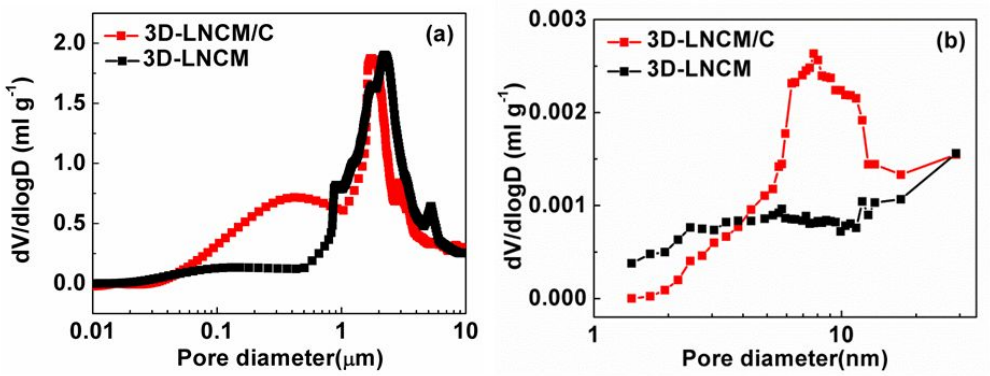

Fig. 3. Pore size distribution curves obtained by (a) mercury intrusion method and (b) nitrogen absorption method for 3D-LNCM and 3D-LNCM/C.

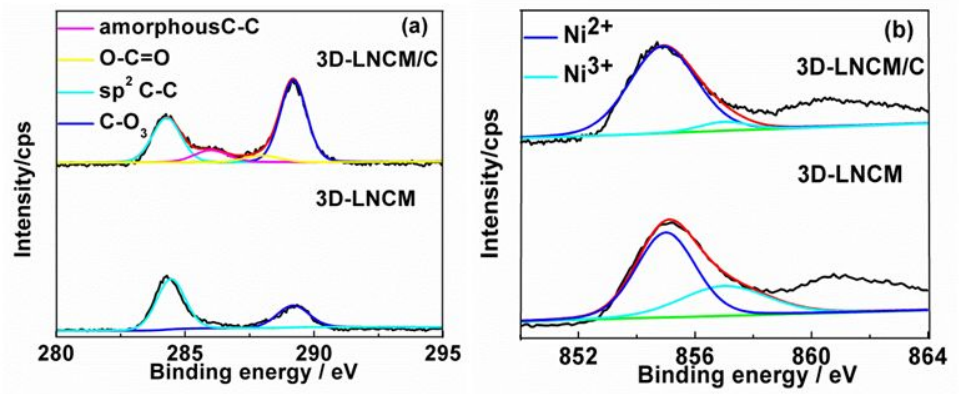

Fig. 4. XPS spectra for C (a), Ni (b) of 3D-LNCM (bottom) and 3D-LNCM/C (upper).

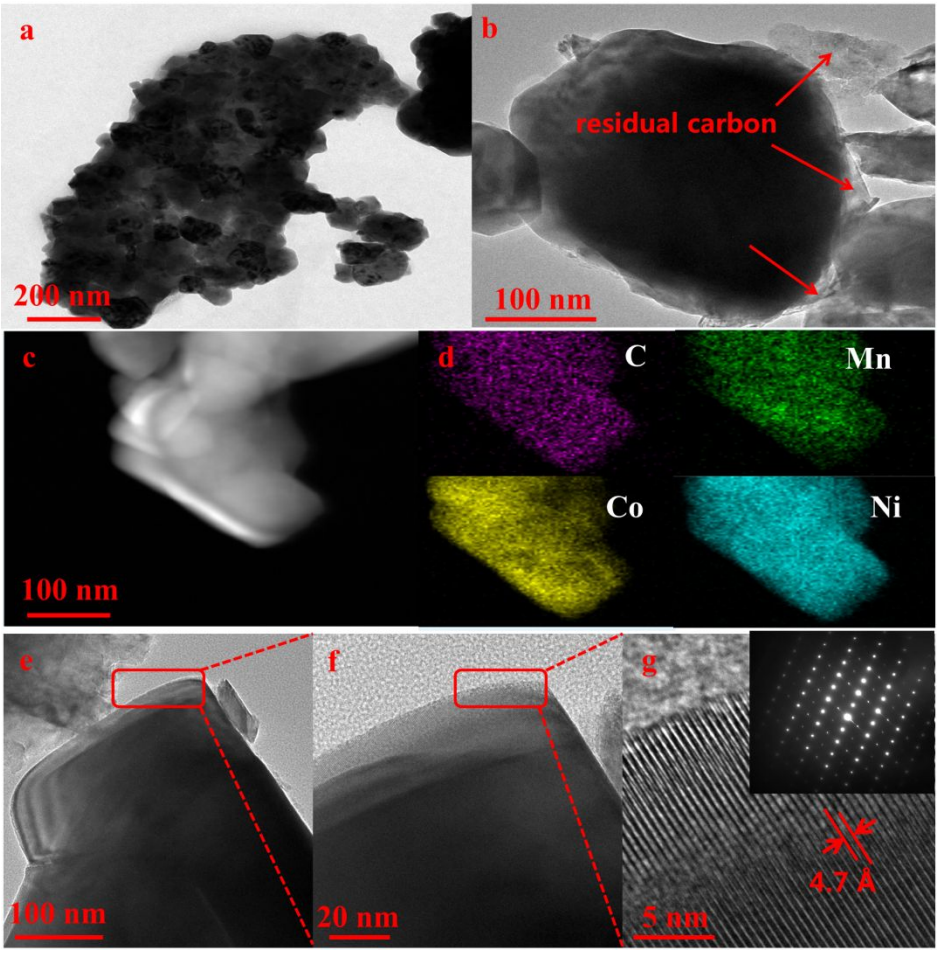

Fig. 5. TEM (a,b), TEM-EDX (c,d) mapping and HR-TEM (e-g) images of 3D-LNCM/C.

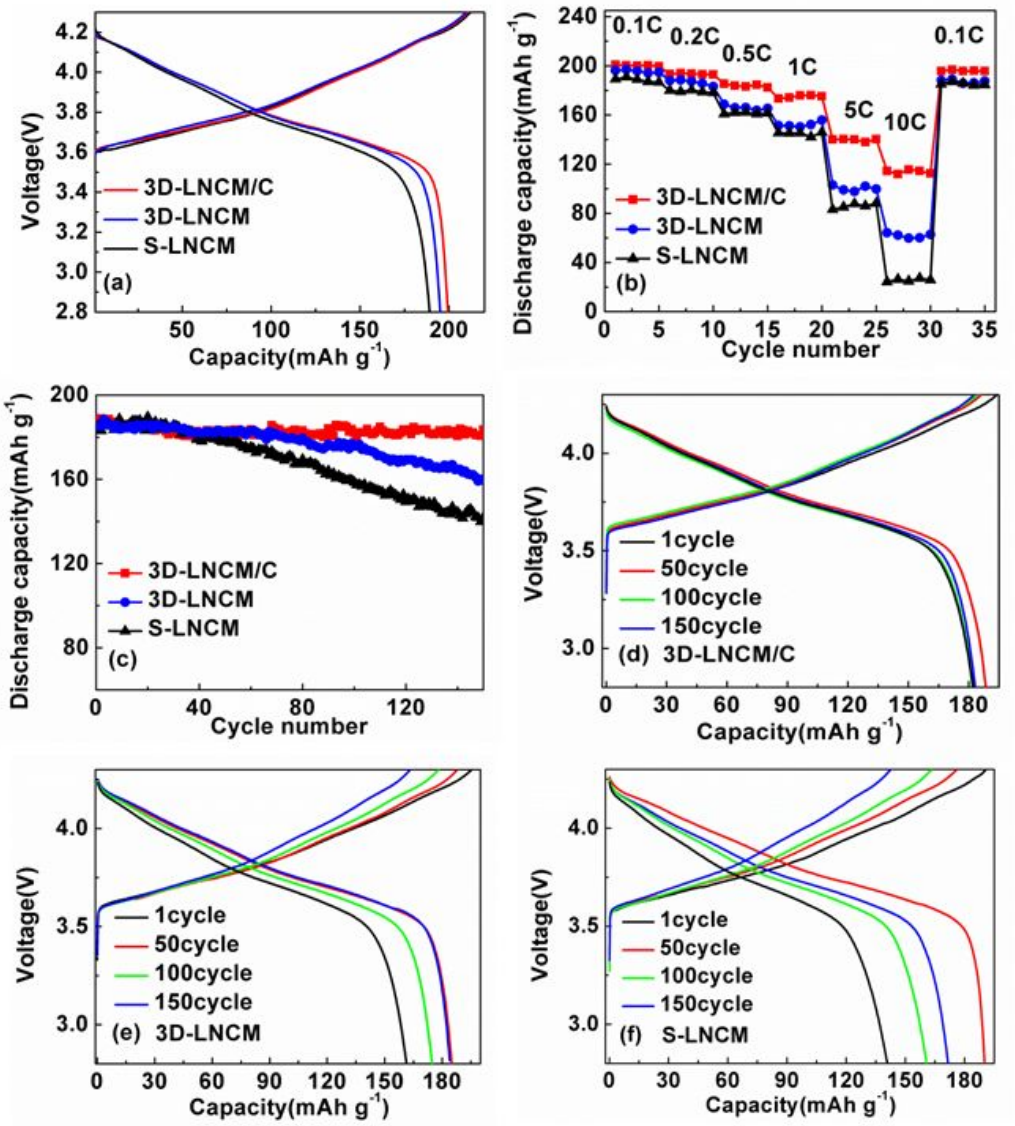

Fig. 6. Electrochemical properties of 3D-LNCM/C, 3D-LNCM and S-LNCM: (a) initial charge-discharge curves at 0.1 C, (b) rate capability, (c) cyclic performanceat 0.2C and (d, e,f) charge-discharge curves at 0.2 C at 1st, 50th, 100th and 150th cycles.

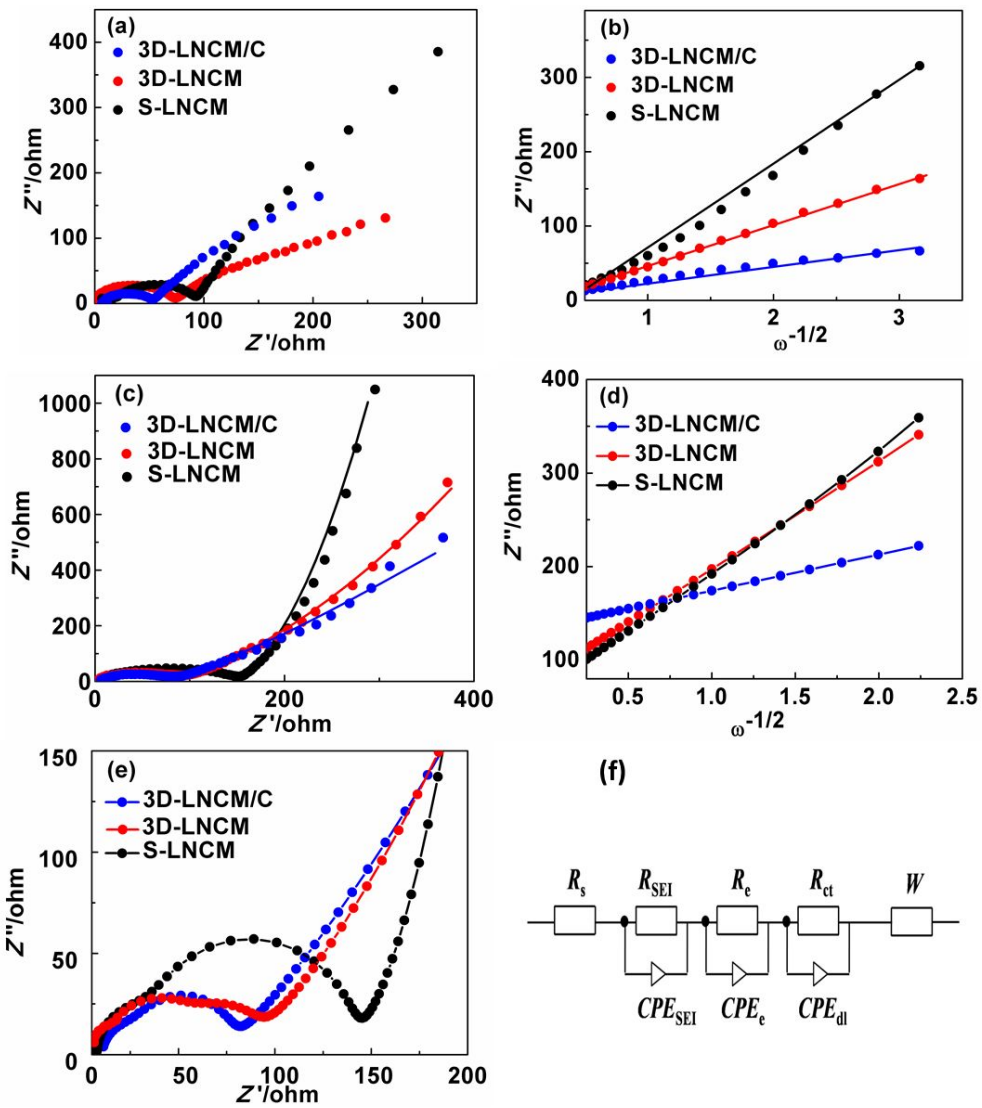

Fig. 7. (a) Nyquist plots of S-LNCM, 3D-LNCM and 3D-LNCM/C after 5 cycles, (b) The relationship between Zre and $\omega^{-1/2}$ at low frequencies after 5 cycles, (c) Nyquist plots after 150 cycles, (d) The relationship between Zre and $\omega^{-1/2}$ at low frequencies after 150 cycles, (e) Nyquist plots at high frequency region after 150 cycles, (f) a corresponding equivalent circuit.

For Table of Contents Only

Abstract graphic